Nano Research

Open Access

Research Article

Synergistic Mo–Ce dual-active sites for high-yield H_2O_2 electrosynthesis via electrochemical oxygen reduction

Song Gao[1,§], Xiang Li[2,§], Weixin Li[2,§], Runjia Xing[2], Jinling Wang[2], Jing Li[3], Jianfu Chen[2]✉, Hehe Wei[2,4]✉, and Wei Du[1]✉

[1] *Shandong University of Aeronautics, Binzhou 256600, China*
[2] *State Key Laboratory of Green Chemical Engineering and Industrial Catalysis, Center for Computational Chemistry and Research Institute of Industrial Catalysis, East China University of Science and Technology, Shanghai 200237, China*
[3] *Engineering Research Center of High-frequency Soft Magnetic Materials and Ceramic Powder Materials of Anhui Province, Engineering Technology Research Center of Preparation and Application of Industrial Ceramics of Anhui Province, School of Chemistry and Material Engineering, Chaohu University, Hefei 238000, China*
[4] *State Key Laboratory of New Ceramic Materials, School of Materials Science and Engineering, Tsinghua University, Beijing 100084, China*
§ *Song Gao, Xiang Li, and Weixin Li contributed equally to this work.*

Cite this article: *Nano Research*, **2026**, *19*, 94908639. https://doi.org/10.26599/NR.2026.94908639

ABSTRACT: Electrochemical oxygen reduction reaction (ORR) for hydrogen peroxide (H_2O_2) synthesis offers a sustainable alternative to the anthraquinone process, yet suffers from inherent activity–selectivity tradeoffs. Herein, this work addresses this challenge through the incorporation of Mo into CeO_2 (Mo-CeO_2) featuring oxygen vacancy-mediated Mo–Ce dual-active sites. Mo incorporation into CeO_2 lattice through hydrothermal defect engineering simultaneously elevates oxygen vacancy concentration and induces localized electron redistribution, creating synergistic sites where Mo atoms facilitate proton donation via spontaneous water dissociation while adjacent Ce centers optimize O_2 adsorption configurations to enhance the intrinsic activity of H_2O_2 generation. *In-situ* characterization and density functional theory calculations reveal that the unique hollow adsorption geometry stabilizes *OOH intermediates and decouples conventional scaling relationships between O_2 adsorption and intermediate binding. This atomic-level cooperativity enables an unprecedented H_2O_2 selectivity of 93%, H_2O_2 yield of 8.2 mol·g_{cat}^{-1}·h^{-1} at 100 mA·cm^{-2}, and exceptional stability. The study establishes an efficient design principle for transition metal oxide catalysts in multi-electron transformations, demonstrating how dual-site engineering can simultaneously enhance intermediate stabilization and reaction kinetics for sustainable electrosynthesis applications.

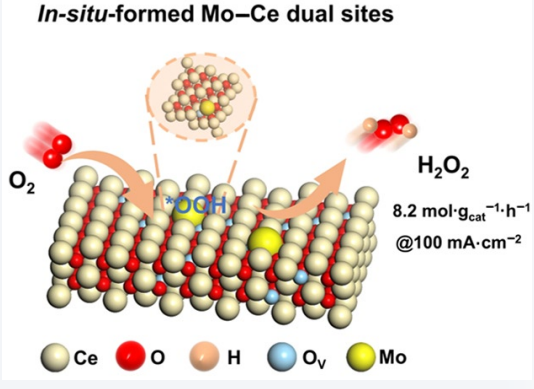

KEYWORDS: hydrogen peroxide, electrocatalysis, dual metal sites, electron distribution, high yield

1 Introduction

Hydrogen peroxide (H_2O_2), an indispensable chemical precursor, plays a pivotal role in environmental remediation, industrial bleaching, and advanced oxidation processes [1, 2]. Contemporary industrial-scale production of H_2O_2 predominantly relies on the anthraquinone process, which suffers from intrinsic limitations, including dependence on palladium-based catalysts, multistep energy-intensive operations, and unavoidable organic solvent contamination [3–6]. Furthermore, centralized manufacturing necessitates hazardous transportation of concentrated H_2O_2 solutions, while downstream purification processes incur substantial economic and environmental costs. In this context, decentralized electrocatalytic two-electron oxygen reduction reaction ($2e^-$ ORR) has emerged as a promising alternative pathway, leveraging renewable energy inputs and enabling on-site H_2O_2 synthesis under ambient conditions [7]. Nevertheless, the practical implementation of the electrocatalytic H_2O_2 synthesis faces dual thermodynamic and kinetic challenges. The competing four-electron ($4e^-$) ORR pathway dominates under most catalytic conditions, fundamentally limiting H_2O_2 selectivity [8]. Moreover, the rational design of selective ORR catalysts is constrained by a

Received: December 23, 2025; **Revised:** February 15, 2026
Accepted: February 15, 2026

✉Address correspondence to Wei Du, duwei@ytu.edu.cn; Hehe Wei, weihh18@tsinghua.org.cn; Jianfu Chen, jfchen@ecust.edu.cn

persistent activity–selectivity tradeoff. This limitation arises from the interdependent adsorption energetics of reaction intermediates, wherein the binding strength of the critical *OOH intermediate cannot be optimized independently. Weak adsorption suppresses the kinetics of O_2 activation, limiting activity, whereas excessively strong binding facilitates O–O bond scission, thereby favoring the complete $4e^-$ reduction to H_2O at the expense of H_2O_2 selectivity [9]. Compounding these issues, the proton-coupled nature of $2e^-$ ORR necessitates efficient water dissociation to supply protons, a frequently overlooked yet critical determinant of overall H_2O_2 yield. These intertwined challenges collectively restrict current electrocatalytic systems to H_2O_2 production rates orders of magnitude below industrial requirements.

Cerium oxide (CeO_2), a prototypical fluorite-structured rare earth oxide, has garnered significant attention for its dynamic redox properties arising from the reversible Ce^{3+}/Ce^{4+} transition, enabling exceptional oxygen storage capacity [10]. The unique characteristic underpins its widespread investigation in diverse electrocatalytic processes, including oxygen evolution reaction (OER) and CO_2 reduction reaction (CO_2RR) [11, 12]. Recent studies on Cu-Ce-O_x solid solutions demonstrated that Ce^{3+}-mediated electron transfer kinetics effectively stabilize Cu^{2+} species, thereby enhancing CH_4 selectivity during CO_2RR [13]. Furthermore, the strategic introduction of oxygen vacancies (O_v) has been identified as an effective approach to modulate surface electronic structures, serving as electron-rich centers for reactant adsorption and activation [14]. The defect engineering strategy is probably advantageous for the ORR, since the integration of Pt clusters onto O_v-rich CeO_2 supports effectively lowered oxygen intermediate adsorption energies and achieved remarkable mass activities of ORR toward H_2O, outperforming conventional Pt/C benchmarks [15]. Despite these merits, inherent material limitations severely constrain the electrocatalytic efficacy of CeO_2 for $2e^-$ ORR. Low intrinsic electronic conductivity, thermodynamic instability of surface vacancies under operational potentials, and nanoparticle sintering during synthesis collectively lead to suboptimal activity and durability [16, 17]. Moreover, the proton-coupled nature of $2e^-$ ORR necessitates efficient water dissociation to supply protons, a process where CeO_2 exhibits inherently sluggish kinetics due to its weak water adsorption energetics. The fundamental limitation creates a critical bottleneck in achieving concurrent O_2 activation and proton supply for sustained H_2O_2 synthesis. Hence, addressing these intertwined challenges through rational engineering of CeO_2-based electrocatalysts thus represents a critical imperative, demanding synergistic resolution of intrinsic material limitations while simultaneously optimizing *OOH intermediate stabilization.

Molybdenum (Mo), a transition metal abundant in nature, exhibits exceptional electrical conductivity and shares analogous electronic characteristics with platinum-group metals, rendering it a compelling candidate for electrocatalytic applications [18]. While traditionally employed in $4e^-$ ORR for fuel cells, merging studies reveal the unique capability of Mo sites to steer the oxygen reduction pathway toward selective hydrogen peroxide generation via the $2e^-$ ORR. Recent advances in Mo-based single-atom catalysts (SACs) with tailored coordination environments (e.g., O and S-coordinated configurations) have demonstrated exceptional $2e^-$ ORR selectivity in alkaline media [19]. First-principles calculations further elucidated that edge-engineered 2H-$MoTe_2$ achieved superior H_2O_2 selectivity by precisely balancing OOH* and O* adsorption energies at zigzag edge sites, thereby thermodynamically favoring $2e^-$ pathway progression while suppressing parasitic $4e^-$ processes [20]. These findings establish Mo as a versatile catalytic platform capable of atomic-level electronic modulation for selective oxygen reduction. Crucially, Mo sites act as efficient active sites for proton donors by accelerating water dissociation kinetics, a critical yet often overlooked requirement for sustained H_2O_2 production, while oxygen vacancies and Ce sites in CeO_2 serve as electron reservoirs to facilitate O_2 activation [21, 22]. The dual-site cooperation mechanism may effectively decouple the traditional activity–selectivity tradeoffs, enabling simultaneous improvements in reaction kinetics and selectivity, and thus significantly enhancing H_2O_2 yields. Therefore, the integration of Mo species with oxygen vacancy-enriched CeO_2 matrices presents a strategic opportunity to synergistically resolve the aforementioned issues of CeO_2 in $2e^-$ ORR for efficient H_2O_2 generation.

Herein, a rationally designed Mo-CeO_2 composite catalyst is fabricated that synergistically integrates molybdenum incorporations and oxygen vacancy-mediated Ce^{3+}/Ce^{4+} redox pairs via a hydrothermal defect-engineering strategy. The dual-active-site architecture addresses the persistent activity–selectivity tradeoff in electrochemical H_2O_2 synthesis by simultaneously enhancing O_2 activation kinetics and stabilizing critical reaction intermediates. Advanced structural characterization confirms that Mo incorporation not only elevates oxygen vacancy concentration compared to pristine CeO_2 but also induces localized electron redistribution. The optimized Mo-CeO_2 catalyst achieves record-breaking H_2O_2 production metrics, with the high yield of 8.2 $mol \cdot g_{cat}^{-1} \cdot h^{-1}$ at 100 $mA \cdot cm^{-2}$ and superior durability, surpassing contemporary noble-metal-free benchmarks. Advanced *in-situ* spectroscopic characterization integrated with density functional theory (DFT) calculation elucidate three synergistic functions of the Mo-CeO_2 system: (i) A distinctive hollow adsorption configuration stabilizes *OOH intermediates (OOH adsorption free energy (ΔG_{OOH}) = −0.51 eV) through dynamically generated Mo–Ce dual sites; (ii) molybdenum centers spontaneously dissociate water to provision protons while adjacent cerium atoms optimize O_2 adsorption geometries; and (iii) crucially, this atomic-level cooperativity disrupts the conventional scaling relationship between O_2 chemisorption energy and *OOH binding affinity.

2 Results and discussion

2.1 Structural characterization of catalysts

Scanning electron microscopy (SEM) images reveal that Mo incorporation preserves the intrinsic nanorod morphology of CeO_2, with both pristine CeO_2 and Mo-CeO_2 exhibiting analogous dimensions (Figs. S1 and S2 in the Electronic Supplementary Material (ESM)). Transmission electron microscopy (TEM) further corroborates the structural retention, demonstrating that Mo-CeO_2 maintains the characteristic fluorite lattice fringes with interplanar spacings of 0.30 and 0.28 nm, corresponding to the (111) and (200) crystal planes of CeO_2, respectively (Figs. 1(a)–1(c)). Notably, the Mo-CeO_2 exhibits a mesoporous architecture, evidenced by interconnected channels permeating the nanorod matrix. Selected atomic intensity analysis of Mo-CeO_2 reveals that discrete Mo atoms (darker spots) occupy substitutional positions of Ce in CeO_2, while maintaining overall fluorite structural integrity (Figs. 1(d) and 1(e)). The absence of MoO_x crystalline phases in high-resolution TEM (HRTEM) images further confirms the atomic-level

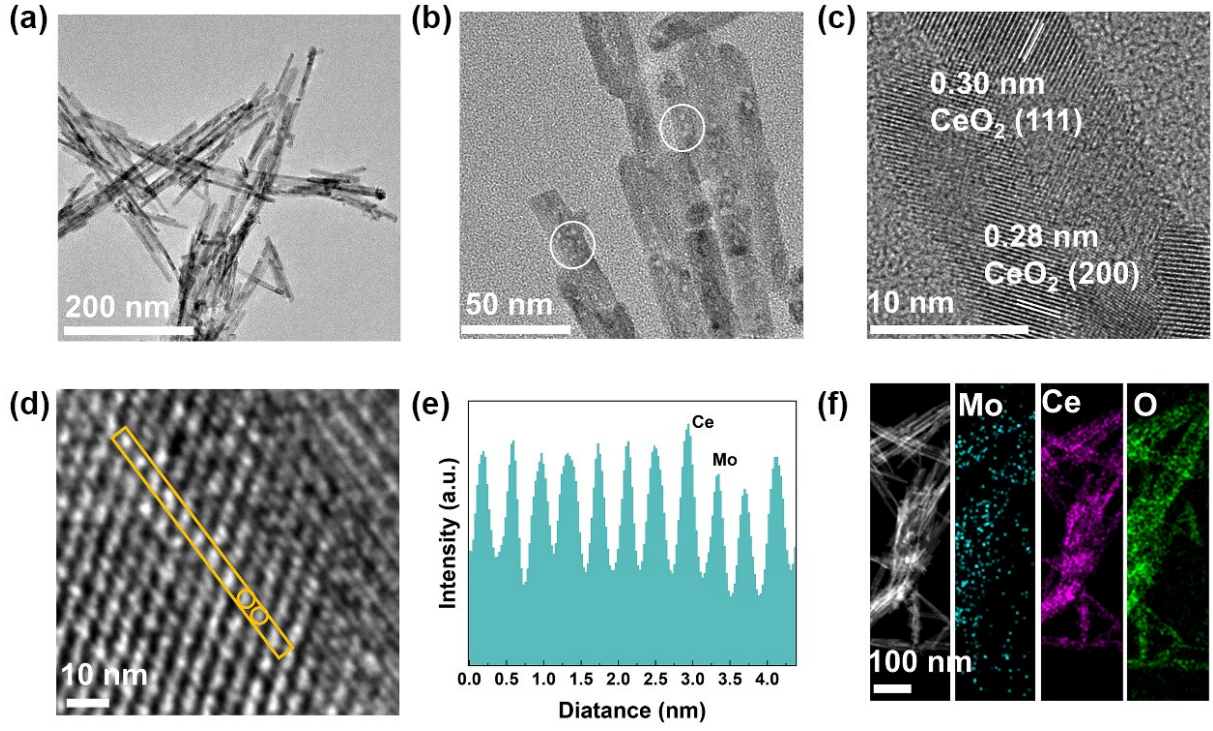

Figure 1 Morphology structure of Mo-CeO_2. ((a)–(d)) TEM images. (e) Selected atomic intensity analysis of (d). (f) Elemental mapping images of Mo, Ce, and O.

dispersion of Mo within the CeO_2 lattice. Energy-dispersive X-ray spectroscopy (EDS) elemental mapping images of Mo-CeO_2 verify the homogeneous distribution of Mo throughout the nanorod framework, with no evidence of agglomeration or phase segregation (Fig. 1(f)).

The hierarchical porosity of Mo-CeO_2, initially observed via TEM, is quantitatively validated through N_2 physisorption analysis. Brunauer–Emmett–Teller (BET) measurements reveal a 44% enhancement in specific surface area for Mo-CeO_2 (70 $m^2 \cdot g^{-1}$) relative to pristine CeO_2 (48 $m^2 \cdot g^{-1}$, Fig. S3(a) and Table S1 in the ESM), directly attributable to the engineered mesoporous architecture. Barrett–Joyner–Halenda (BJH) pore size distribution analysis confirms uniform mesopores (Fig. S3(b) in the ESM), consistent with TEM-derived structural parameters. The synergistic combination of high surface area and well-defined mesoporosity serves dual functions: (i) maximizing exposure of Mo–Ce dual-active sites through reduced particle agglomeration, and (ii) establishing rapid mass transport channels that suppress parasitic H_2O_2 reduction via shortened reactant and product diffusion lengths [23, 24].

The atomic-level dispersion and substitutional doping of Mo within the CeO_2 lattice are confirmed by converging evidence from multiple techniques. In Fig. 2(a), X-ray diffraction (XRD) patterns of both Mo-CeO_2 and pristine CeO_2 exhibit characteristic reflections of the cubic fluorite phase (PDF#34-0394), with no detectable peak shifts or secondary phases, confirming lattice parameter preservation despite Mo incorporation. The absence of crystalline molybdenum phases in XRD patterns, coupled with inductively coupled plasma mass spectrometry (ICP-MS) quantification of Mo loading in Mo-CeO_2 (0.52 wt.%), rules out the formation of nanoparticles or secondary phases and corroborates Mo incorporation at the atomic level without phase segregation [25]. This is further supported by Raman spectroscopy. For pristine CeO_2, the dominant Raman peak at 464 cm^{-1} is associated with the symmetric Ce–O stretching vibrations (F_{2g}) in fluorite CeO_2 [26], and the peak at 600 cm^{-1} originates from the existence of oxygen vacancy (D, Fig. 2(b)). After the incorporation of Mo into CeO_2, the F_{2g} mode undergoes significant intensity attenuation and a redshift in Mo-CeO_2 compared with that of pristine CeO_2. The phenomenon arises from Mo-induced lattice distortion and localized charge imbalance [26, 27]. Concurrently, the emergence of a distinct vibrational mode at 795 cm^{-1} in Mo-CeO_2, assigned to Mo–O stretching, directly evidences successful Mo element integration into CeO_2. The conclusion is further confirmed by ultraviolet–visible (UV–Vis) diffuse reflectance spectroscopy of pristine CeO_2 and Mo-CeO_2, where a 30 nm redshift in the absorption edge from 434 nm for pristine CeO_2 to 464 nm for Mo-CeO_2 owing to the interaction between Mo and CeO_2 (Fig. S4 in the ESM) [28].

The electronic structure and defect chemistry of Mo-CeO_2 were rigorously interrogated through high-resolution X-ray photoelectron spectroscopy (XPS). Deconvolution of the Mo 3d spectrum in Mo-CeO_2 (Fig. 2(c)) confirms that molybdenum is predominantly present in the 6+ oxidation state (peaks at 232.3 and 235.6 eV), which is characteristic of its substitutional incorporation into the CeO_2 lattice [29]. This primary assignment of Mo^{6+} is central to the proposed doping mechanism. Conclusive evidence for this mechanism is provided by the corresponding Ce 3d spectra (Fig. 2(d)). The XPS spectra of Ce 3d in Mo-CeO_2 are mainly fitted and divided into four groups of peaks, namely $3d_{3/2}$ and $3d_{5/2}$. Among these, U‴, V‴, U, V, U″, and V″ are the peaks corresponding to Ce^{4+}; meanwhile, U′ and V′ belong to the peaks of Ce^{3+} (Fig. 2(d)) [30–32]. Quantitative analysis reveals a substantial increase in the $Ce^{3+}/(Ce^{3+} + Ce^{4+})$ ratio for Mo-CeO_2 compared to pristine CeO_2 (Table S2 in the ESM). This increase is stoichiometrically consistent with the charge compensation required when Mo^{6+} substitutes for Ce^{4+}, formally described by the defect equilibrium. This direct correlation between Mo

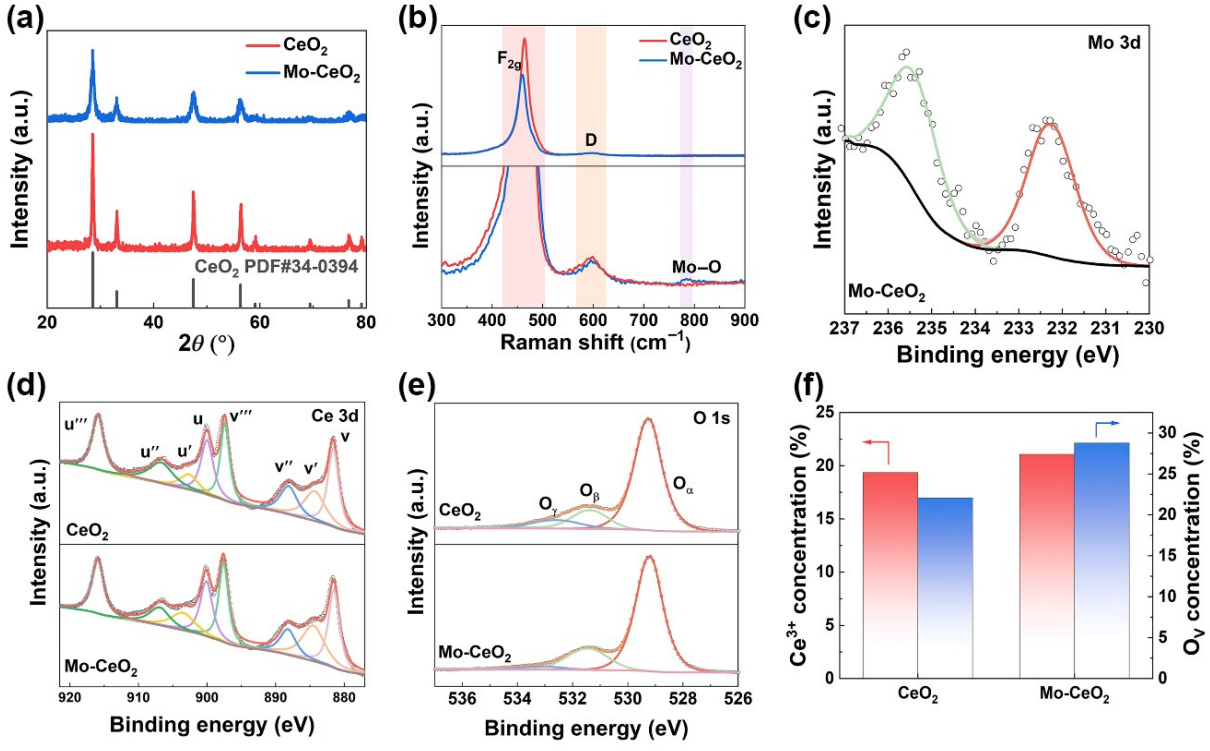

Figure 2 Phase and electronic structures of Mo-CeO_2 and pristine CeO_2. (a) XRD patterns. (b) Raman spectra. (c) Mo 3d XPS spectrum of Mo-CeO_2. (d) Ce 3d XPS spectra. (e) O 1s XPS spectra. (f) Concentration of Ce^{3+}, O_v of Mo-CeO_2, and pristine CeO_2.

incorporation and Ce^{3+} formation strongly supports atomic-scale substitutional incorporation rather than cluster formation.

The O 1s XPS spectra analysis provides compelling evidence for the vacancy-mediated structural modifications in Mo-CeO_2 (Fig. 2(e)). The spectral deconvolution of Mo-CeO_2 reveals three distinct components of lattice oxygen (O_α, 529.2 eV), oxygen vacancies (O_β, 531.4 eV), and surface-adsorbed oxygen species (O_γ, 532.8 eV) [33]. Notably, an increase in the $O_\beta/(O_\alpha + O_\beta)$ intensity ratio for Mo-CeO_2 compared to that of pristine CeO_2, quantitatively confirming the oxygen vacancy enrichment induced by molybdenum incorporation (Fig. 2(f) and Table S3 in the ESM). The retained lattice oxygen component of O_α maintains comparable binding energies, indicating preserved fluorite framework integrity despite enhanced defect density. Electron paramagnetic resonance (EPR) spectroscopy was employed to directly quantify the paramagnetic oxygen vacancies, providing definitive evidence for the defect structures modulated by Mo incorporation. As shown in Fig. S5 in the ESM, pristine CeO_2 exhibits only a negligible EPR signal, consistent with its low intrinsic defect concentration. In stark contrast, the Mo-CeO_2 catalyst displays a pronounced symmetric signal, which is the characteristic signature of unpaired electrons localized in oxygen vacancies [34, 35]. Therefore, the integration of Mo atoms and the elevated concentration of oxygen vacancies are fabricated in Mo-CeO_2, which probably enables it with preeminent electrocatalytic performances in the ORR to generate H_2O_2 [36, 37].

2.2 Electrocatalytic performance of Mo-CeO_2

The electrochemical ORR properties of Mo-CeO_2 and pristine CeO_2 were assessed using a rotating ring-disk electrode (RRDE), with charge transfer coefficients (N) calibrated through potassium ferricyanide probe method (Fig. S6 in the ESM). The linear sweep voltammetry (LSV) curves reveal that Mo-CeO_2 demonstrates substantially enhanced ring current density across a wide potential window of 0–0.7 V vs. reversible hydrogen electrode (RHE) compared with pristine CeO_2 (Fig. 3(a)), coupled with the superior O_2 activation capability of Mo-CeO_2 (Fig. S7 in the ESM), indicating superior electrocatalytic activity for hydrogen peroxide generation. Quantitative evaluation of the reaction pathway through polarization curve analysis confirms the exceptional selectivity of Mo-CeO_2 for $2e^-$ ORR process (Figs. 3(b) and 3(c)). The Mo-CeO_2 catalyst achieves a remarkable selectivity of 93% for H_2O_2 production at 0.43 V vs. RHE (Fig. S8 in the ESM), maintaining H_2O_2 selectivity above 90% throughout the 0–0.5 V potential range. The corresponding electron transfer number (n) approximates 2.0 across the tested potentials, confirming the dominant $2e^-$ reduction mechanism of Mo-CeO_2. These electrochemical metrics establish that molybdenum incorporation effectively modulates the oxygen reduction pathway in CeO_2, suppressing competitive $4e^-$ oxygen reduction while promoting selective hydrogen peroxide formation.

To establish a definitive structure–activity relationship, we systematically investigated the influence of Mo doping concentration on the electrocatalytic performance. A series of Mo-CeO_2 catalysts with precisely controlled Mo loadings (0.44 wt.%–0.60 wt.%, determined by ICP-optical emission spectroscopy (ICP-OES) were synthesized via a hydrothermal defect-engineering approach. RRDE measurements show that the disk current density increases with Mo content (Fig. S9 in the ESM), indicating enhanced O_2 adsorption and activation kinetics. Crucially, the selectivity towards H_2O_2 exhibits a pronounced volcano-shaped dependence on Mo loading (Figs. S10 and S11 in the ESM), reaching an optimal value of ~ 93% at 0.4 V vs. RHE for the 0.52 wt.% catalyst. This non-monotonic trend underscores the

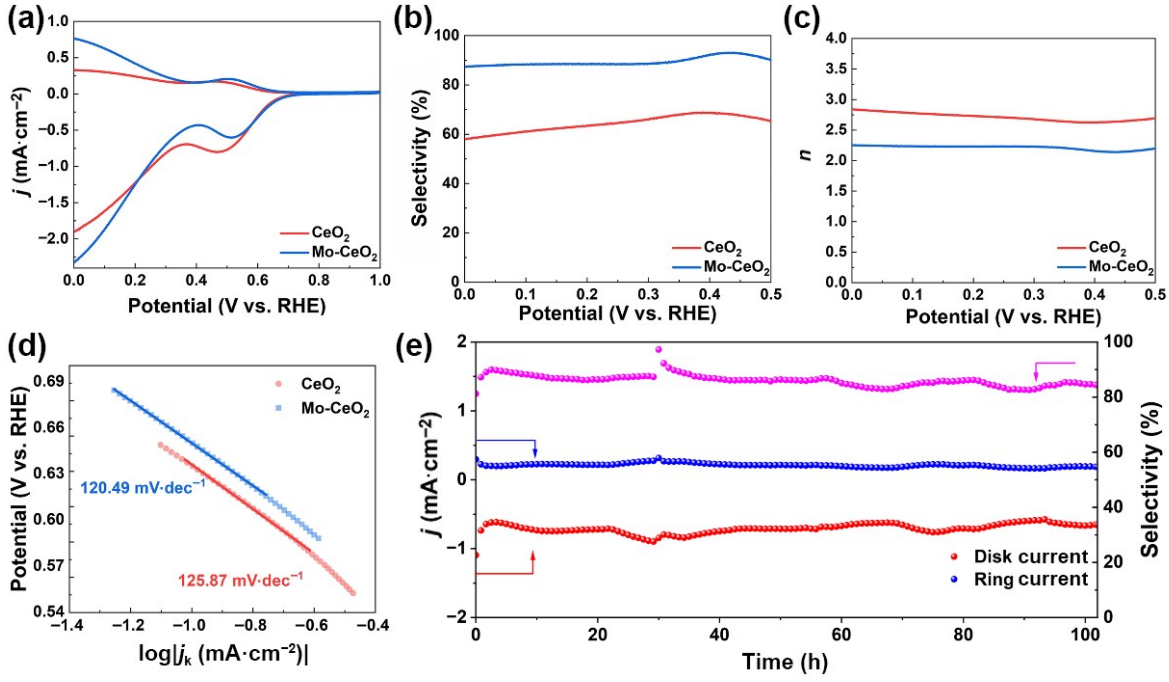

Figure 3 Electrochemical performances of Mo-CeO_2 and pristine CeO_2 in O_2-saturated 0.1 M KOH using a RRDE. (a) LSV curves (upper part: ring current density and bottom part: disk current density). (b) H_2O_2 selectivity. (c) Electron transfer numbers. (d) Tafel plots. (e) Stability curves of Mo-CeO_2.

necessity for a critical balance in tailoring the surface electronic structure. The subsequent decline in selectivity at the upper limit of the achievable atomic-dispersion range (0.60 wt.%) is highly instructive, as our synthesis method reached its limit for effective lattice incorporation beyond this loading. Strikingly, the trend in H_2O_2 selectivity aligns perfectly with the concentration of paramagnetic oxygen vacancies directly quantified by EPR spectroscopy (Fig. S5 in the ESM), which also peaks at 0.52 wt.% Mo. This quantitative correlation provides a definitive materials-based explanation: The superior performance is fundamentally linked to an optimal population of oxygen vacancies, which electronically tailors the Mo–Ce dual sites to ideally stabilize the *OOH intermediate for the 2e⁻ pathway. The distinct volcano relationship within the accessible doping window conclusively demonstrates that precise control of the incorporation concentration is paramount for maximizing the selective H_2O_2 synthesis activity of metal‑oxide catalysts.

The 2e⁻ ORR kinetics were elucidated through Tafel analysis derived from polarization curve data (Fig. 3(d)), with kinetic current density for H_2O_2 generation plotted against overpotentials. The Mo-CeO_2 catalyst exhibits a Tafel slope of 120.49 mV·dec^{-1}, markedly lower than pristine CeO_2 (125.87 mV·dec^{-1}), demonstrating enhanced kinetic propensity for the 2e⁻ ORR pathway in Mo-CeO_2 [24]. To quantify the number of electrochemically accessible sites and evaluate the intrinsic activity, the electrochemical surface area (ECSA) was estimated (Figs. S12–S14 in the ESM). The calculated double-layer capacitance (C_{dl}) and corresponding ECSA values are presented in Fig. S14 in the ESM. Normalization of the H_2O_2 partial current density to the ECSA (Fig. S15 in the ESM) reveals that Mo-CeO_2 exhibits a 1.2-fold higher specific activity compared to pristine CeO_2 at 0 V vs. RHE. This demonstrates a superior intrinsic activity per accessible site, which we attribute to the optimized electronic structure resulting from Mo incorporation and associated oxygen vacancies. The improvement indicates the electronic structure modification induced by optimal Mo incorporation, which enhances active site efficiency. Further mechanistic validation was obtained through hydrogen peroxide reduction reactions (H_2O_2RR) evaluations in 0.1 M KOH containing 10 mM H_2O_2. The significantly attenuated reduction current density of Mo-CeO_2 confirms its negligible H_2O_2RR activity (Fig. S16 in the ESM). The kinetic inertia toward H_2O_2 decomposition effectively prevents parasitic decomposition of synthesized H_2O_2 during ORR operation, thereby ensuring exceptional product retention. The combined kinetic and mechanistic evidence establishes that molybdenum incorporation simultaneously optimizes oxygen activation thermodynamics while passivating undesired peroxide consumption pathways, achieving an ideal balance for sustainable H_2O_2 electrosynthesis.

Building upon its demonstrated selectivity and kinetic advantages, the operational durability of the Mo-CeO_2 catalyst was rigorously evaluated under continuous ORR conditions. Chronoamperometric stability assessment conducted at 0.33 V vs. RHE for an extended period of 102 h reveals exceptional robustness (Fig. 3(e)). Both the disk and ring current densities show negligible attenuation, while the selectivity for H_2O_2 production consistently remains above 80% throughout the test. To probe the origin of this stability, comprehensive post-test characterization was performed. High-resolution XPS analysis of the spent catalyst (Fig. S17 in the ESM) confirms that the chemical states of Ce (Ce^{3+}/Ce^{4+}), Mo (dominant Mo^{6+}), and O (lattice oxygen/vacancy distribution) remain virtually identical to those of the fresh catalyst. This structural and chemical preservation under prolonged operation is attributed to the robust framework integrity of the Mo-CeO_2 system. The confluence of sustained activity, uncompromised selectivity over extended operation, and retained structural identity establishes Mo-CeO_2 as a highly durable electrocatalyst prototype, demonstrating significant potential for practical H_2O_2 electrosynthesis.

The practical H_2O_2 synthesis capability of Mo-CeO_2 was systematically investigated using a gas-diffusion electrode flow cell

system, with peroxide quantification conducted via cerimetric titration (Fig. S18 in the ESM), which transcends the inherent oxygen mass transfer limitations of conventional H-cell configurations. In Fig. 4(a), Mo-CeO_2 demonstrates exceptional potential-dependent current response, achieving a mass-transport-corrected current density of −109 mA·cm^{-2} at 0 V vs. RHE, which shows 1.6-fold current densities relative to pristine CeO_2 under identical conditions. Steady-state electrolysis across various current densities (25 to 100 mA·cm^{-2}) reveals remarkable catalytic performance metrics (Figs. 4(b) and 4(c)). The optimized Mo-CeO_2 catalyst sustains H_2O_2 production rates exceeding 2.0 mol·g_{cat}^{-1}·h^{-1} with concomitant Faradaic efficiencies (FE) > 87% throughout the operational window. Notably, the remarkable catalytic ability of Mo-CeO_2 for H_2O_2 production reaches a promising yield of 8.2 mol·g_{cat}^{-1}·h^{-1} at 100 mA·cm^{-2}, indicating its astonishing performances and potential for scale-up applications. The stark performance contrast with pristine CeO_2 indicates the critical role of molybdenum-induced electronic modulation. The performance of Mo-CeO_2 is benchmarked against state-of-the-art 2e$^-$ ORR electrocatalysts (Table S4 in the ESM and Fig. 4(d)). While differences in experimental systems exist across studies, Mo-CeO_2 achieves competitive performance under the evaluated conditions. Particularly in alkaline flow-cell configurations, it matches or surpasses most reported noble-metal-free catalysts in both H_2O_2 production rate and Faradaic efficiency [4, 38–50], as evidenced by the high yields at multiple applied potentials (e.g., 0.3 and 0.5 V vs. RHE). This underscores that the oxygen vacancy-mediated synergistic dual-active-site mechanism effectively optimizes the Sabatier relationship for 2e$^-$ pathway dominance.

To assess practical viability, the Mo-CeO_2 catalyst was subjected to extended galvanostatic operation at an industrially significant current density of 75 mA·cm^{-2} in the gas-diffusion flow cell configuration (Fig. 4(e)). The Mo-CeO_2 catalyst maintains a sustained H_2O_2 production rate of > 6 mol·$g_{catalyst}^{-1}$·h^{-1} with Faradaic efficiency exceeding > 80% throughout the stability test, accumulating 33.7 mol·g_{cat}^{-1} of peroxide product within 5 h. The chronopotentiometric (voltage–time (*E*–*t*)) profile of Mo-CeO_2 exhibits negligible degradation during the stability assessment, further demonstrating its exceptional durability and decay resistance (Fig. S19 in the ESM). Post-stability operational characterizations reveal the remarkable structural preservation of Mo-CeO_2. XRD analysis confirms the retention of the cubic fluorite phase without secondary phase formation (Fig. S20 in the ESM), while HRTEM images show intact rod-like morphology with preserved atomic dispersion of Mo incorporation within the CeO_2 matrix (Fig. S21 in the ESM). These results collectively validate the exceptional operational stability of the Mo-CeO_2 catalyst, underpinned by its structural preservation and sustained FE during extended high-current operation. The synergistic interplay between molybdenum incorporation and the ceria matrix establishes a robust materials platform for industrial-scale electrocatalytic H_2O_2 synthesis, demonstrating practical viability.

The selectivity paradigm in 2e$^-$ oxygen reduction is fundamentally correlated with the stabilization of *OOH intermediates on Mo-CeO_2 surfaces. To elucidate the reaction dynamics, *in-situ* attenuated total reflection surface-enhanced infrared absorption spectroscopy (ATR-SEIRAS) analysis was conducted during 2e$^-$ ORR operation (Fig. 4(f)). The distinct vibrational signatures for Mo-CeO_2 emerge at 1250 cm^{-1}, corresponding to the O–O stretching mode of surface-adsorbed *OOH species [51, 52]. Furthermore, the peak observed at approximately 1460 cm^{-1} [53, 54] is assigned to the O–O stretching vibration of adsorbed superoxide species (O_2^-), a direct precursor to OOH formation. The progressive intensification of both bands at more cathodic potentials (from 1.0 to 0 V vs. RHE) maps the continuous reaction pathway from O_2 activation to *OOH stabilization on the active sites. To unequivocally attribute this capability to the Mo–Ce dual sites, a control experiment on pristine

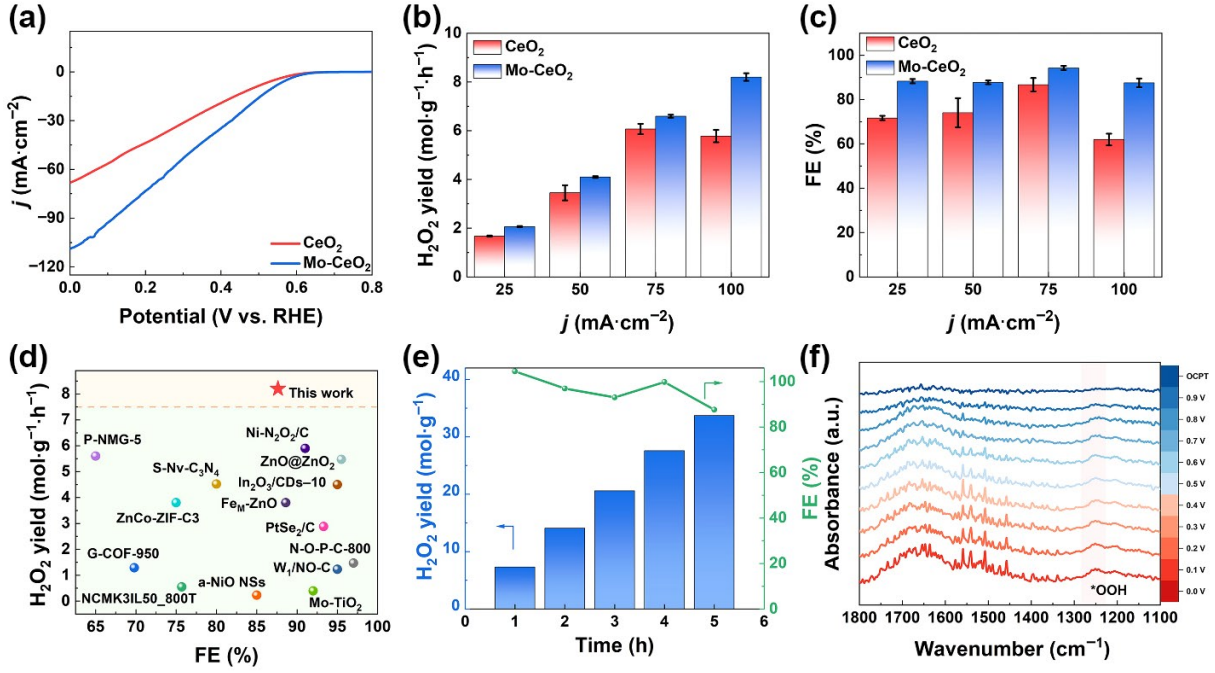

Figure 4 Electrochemical synthesis of H_2O_2 over Mo-CeO_2 and pristine CeO_2 in a flow-cell. (a) LSV curves. (b) H_2O_2 production under various current densities from 25 to 100 mA·cm^{-2}. (c) FE values. (d) Comparison 2e$^-$ ORR performances of Mo-CeO_2 with recently reported electrocatalysts in flow-cell. (e) Stability test of H_2O_2 yields and FE over Mo-CeO_2 at 75 mA·cm^{-2}. (f) *In-situ* ATR-SEIRAS spectra of Mo-CeO_2 in 0.1 M KOH.

CeO_2 was conducted under identical conditions (Fig. S22 in the ESM). Its spectra show no significant evolution in the critical ~ 1250 cm^{-1} region, starkly contrasting with the pronounced signals on Mo-CeO_2. This direct comparison confirms that pristine CeO_2 cannot effectively stabilize the *OOH intermediate, highlighting the indispensable role of Mo incorporation. The observed spectroscopic evolution provides direct experimental validation of the synergistic mechanism proposed from theory. The potential-dependent buildup of *OOH coverage correlates with its optimized adsorption energy on the Mo–Ce dual sites, which is the crucial descriptor for $2e^-$ pathway dominance. This configuration, enabled by oxygen vacancy-mediated electronic modulation, synergistically enhances O_2 activation (evidenced by $*O_2^-$ formation) while tuning the *OOH binding strength to prevent O–O bond cleavage, thereby steering the reaction selectively toward H_2O_2.

To elucidate the reaction pathway and underlying $2e^-$ ORR mechanism governing the catalyst, systematic DFT calculations were conducted to investigate ORR processes on pristine CeO_2 and Mo-CeO_2 surfaces. The elucidated ORR pathways, corresponding Gibbs free energy profiles at applied potentials of 0 and 0.68 V, along with optimized adsorption configurations for key intermediates, are presented in Figs. 5(a)–5(c) and Fig. S23 and Table S5 in the ESM, respectively. Within the Mo-CeO_2 structure, Mo substitution at a surface Ce lattice site spontaneously generates a surface oxygen species bound to Mo, exhibiting a favorable formation energy of −0.81 eV. This is consistent with experimental

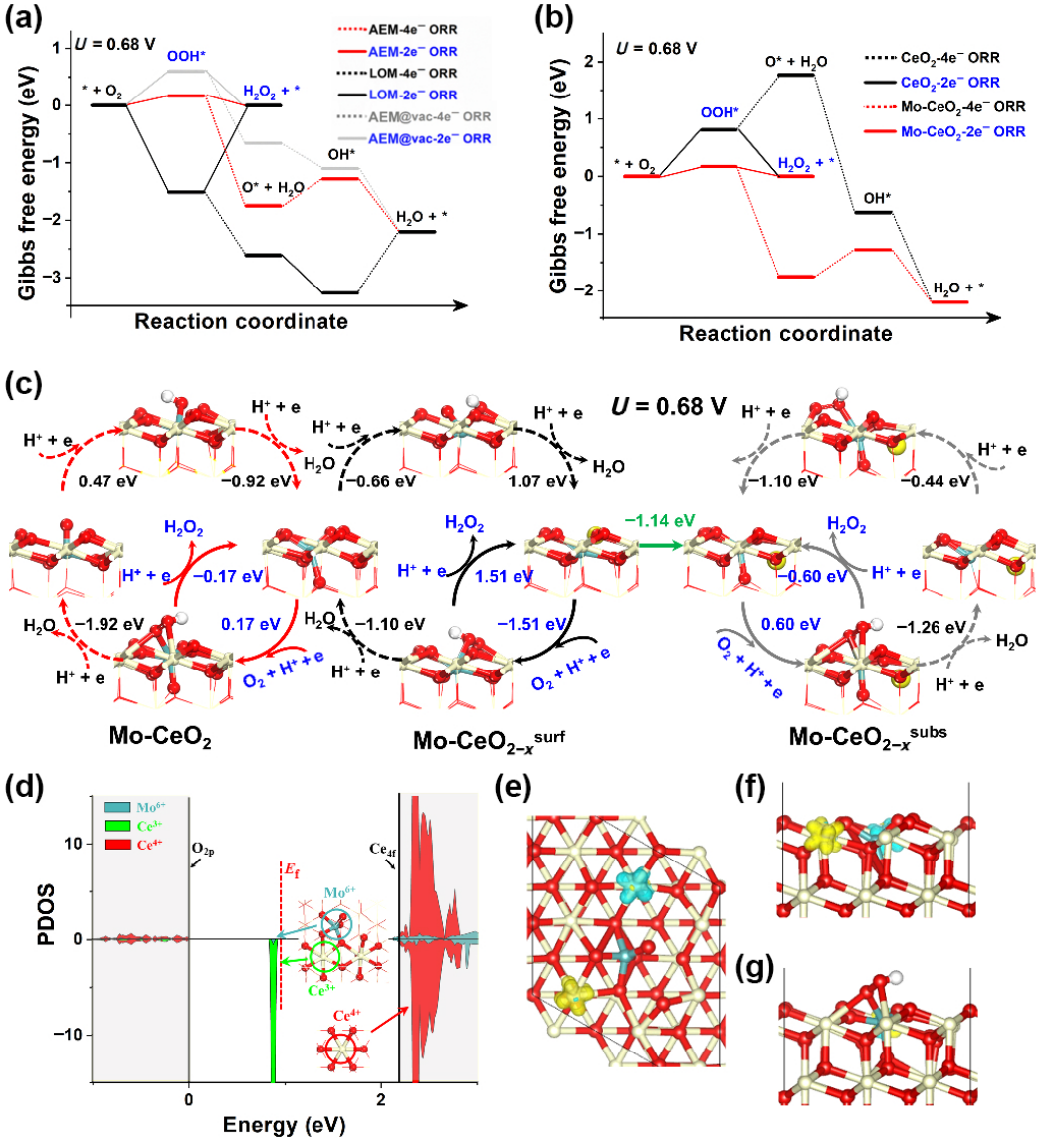

Figure 5 DFT calculations of pristine CeO_2 and Mo-CeO_2 for the ORR processes. (a) Reaction coordinates for the ORR processes of possible structures in Mo-CeO_2 at the applied potential of 0.68 V, including Mo-CeO_2 with AEM (red line), Mo-CeO_{2-x}^{surf} with LOM (black line), and Mo-CeO_{2-x}^{subs} with AEM@vac mechanisms (gray line). (b) Reaction pathways for the ORR processes on Mo-CeO_2 (red line) and pristine CeO_2 (black line) at 0.68 V. (c) Reaction pathways and corresponding optimized adsorption structures of the intermediates during the ORR processes on Mo-CeO_2, Mo-CeO_{2-x}^{surf}, and Mo-CeO_{2-x}^{subs}. (d) The local density of states for pristine CeO_2 and Mo-CeO_2, which are projected on the f-orbital of surface Ce (green/red) and the d-orbital of the surface Mo (blue), where the black lines are the total DOS of the corresponding systems for reference. Red dotted line is E_f, and all the energies are aligned to the vacuum level and E_f of the CeO_2 (111) surface is aligned to 0 eV. The isosurface (0.005) of calculated spin charge densities. (e) Top view of Mo-CeO_2. (f) Side view of Mo-CeO_2. (g) Side view of Mo-CeO_2 with OOH adsorption. White, red, and light-yellow balls represent H, O, and Ce atoms, while the surface and subsurface O vacancy is particularly marked in yellow.

XPS characterization indicating Mo^{6+}. Under oxygen reduction reaction conditions, the surface-bound oxygen species coordinated to Mo undergoes facile protonation followed by dehydration to yield an active Mo site, characterized by Gibbs free energy changes of −1.81 eV at 0.0 V and −0.42 eV at 0.68 V according to the elementary reaction of $O^* + 2H^+ + 2e^- \rightarrow H_2O + *$. This catalytically active configuration, comprising the surface Mo and two adjacent Ce atoms, arises specifically through this activation pathway and facilitates the proton-coupled adsorption of O_2 to form a distinctive OOH intermediate with a corresponding adsorption energy of −0.51 eV (Fig. 5(c), red cycle). DFT simulations confirm this specific OOH^* geometry is inaccessible on the pristine CeO_2 surface. The subsequent protonation of OOH^* on the Mo-CeO_2 surface yields either H_2O_2 or H_2O plus an adsorbed O^* intermediate on Mo sites, with Gibbs free energy changes of −0.86 and −2.60 eV, respectively. The analysis of the reaction coordinate (Fig. S23(a) in the ESM, red lines) confirms all elementary steps are exergonic at Mo-CeO_2 surface, adhering to an adsorbate evolution mechanism (AEM).

Notably, the Mo-CeO_2 surface exhibits the reduced formation energies for surface (1.86 eV) and subsurface (0.72 eV) oxygen vacancies (denoted as Mo-CeO_{2-x}^{surf} and Mo-CeO_{2-x}^{subs}) compared to pristine CeO_2 (1.95 eV), aligning with experimental observations of enhanced vacancy concentration. In the Mo-CeO_{2-x}^{surf} configuration, the surface vacancy directly participates in the ORR cycle via a lattice oxygen oxidation mechanism (LOM). This involvement significantly strengthens the adsorption of oxygen-containing intermediates, as nascent oxygen species are stabilized through occupation of the vacancy site and concomitant bonding to the Mo and dual Ce_{6c} atoms (Fig. 5(c), black cycle). Hence, the free energies of the preceding conversion reactions ($O_2 + 3H^+ + 3e^- \rightarrow OH^* + 2H_2O$) at Mo-$CeO_{2-x}^{surf}$ in the ORR are obviously exothermic (Fig. 5(a), black lines). However, the resulting pronounced adsorption strength renders the desorption of subsequent OOH^*/OH^* intermediates endergonic, ultimately diminishing ORR activity relative to the Mo-CeO_2 surface. For the thermodynamically favored Mo-CeO_{2-x}^{subs} configuration, the subsurface vacancy cannot directly participate in the ORR cycle, demonstrating the AEM at Mo/CeO_{2-x}^{subs} (AEM@vac). The lattice relaxation induced by the subsurface vacancy results in Mo adopting a stable tetrahedral coordination with underlying and surface oxygen atoms, enhancing vacancy stability with −1.14 eV relative to the surface vacancy (Fig. 5(c), grey cycle). This induces the weaker intermediate binding, evidenced by a slightly exergonic OOH^* adsorption energy of −0.08 eV, and consequently lower ORR activity (Fig. 5(a), grey line). Therefore, the optimal ORR catalytic activity for Mo-CeO_2 arises from *in-situ* dynamically generated Mo–Ce dual sites on the Mo-CeO_2 surface during the ORR process.

Crucially, the maximum increase in free energy within the potential-limiting step of the $4e^-$ ORR pathway within the Mo-CeO_2 structure ($OOH^* + 3H^+ + 3e^- \rightarrow 2H_2O + *$) manifests during the third step ($O + H^+ + e^- \rightarrow OH^*$, $\Delta G = -0.21$ eV). This value is less favorable than the corresponding step in the $2e^-$ pathway ($OOH^* + H^+ + e^- \rightarrow H_2O_2 + *$, $\Delta G = -0.86$ eV), strongly favoring H_2O_2 production over complete reduction to H_2O. In contrast, pristine CeO_2 exhibits endergonic initial protonation steps ($O_2 + H^+ + e^- \rightarrow OOH^*$ and $OOH^* + H^+ + e^- \rightarrow O^* + H_2O$), indicative of unfavorable O^* adsorption thermodynamics (Fig. 5(b), black profile). Consequently, OOH^* predominantly undergoes direct protonation to H_2O_2. The weak adsorption energy of OOH^* at Ce sites renders its formation kinetically challenging, establishing it as the potential-determining step (PDS) for the $2e^-$ ORR pathway [55]. Figures 5(b) and 5(c) further identify the adsorption of O_2 as the PDS for the $2e^-$ ORR on both pristine CeO_2 and Mo-CeO_2 catalysts, exhibiting limiting potentials of 0.13 and −0.51 eV, respectively. The theoretical overpotentials (η) relative to the equilibrium potential ($U = 0.68$ V) for this pathway are calculated as 0.81 and 0.17 eV for the respective catalysts. This pronounced reduction in overpotential demonstrates the superior intrinsic activity of the Mo-CeO_2 catalyst toward selective H_2O_2 generation, a finding in excellent agreement with experimental observations.

Furthermore, under alkaline conditions, the negligible concentration of solvated protons (e.g., pH = 13 and $C_{H^+} = 10^{-13}$, where C_{H^+} is the concentration of hydrogen ions in aqueous solution) necessitates an alternative proton source for the oxygen reduction reaction. Hence, the energy barrier associated with water dissociation frequently serves as a critical activity descriptor in alkaline electrocatalysis, analogous to hydrogen evolution studies [56]. To elucidate proton supply kinetics for $2e^-$ ORR, the energetics of H_2O dissociation on pristine CeO_2 and Mo-CeO_2 surfaces were computationally evaluated. On pristine CeO_2, water adsorption free energy is weak ($G_{ads} = -0.07$ eV), with dissociative adsorption exhibiting minimal exergonicity ($\Delta G_{diss} = -0.11$ eV). In stark contrast, the Mo-CeO_2 surface facilitates spontaneous water dissociation, evidenced by a significantly enhanced dissociative adsorption free energy of −0.59 eV (Fig. S24 in the ESM). Thermodynamically, H_2O dissociative adsorption on the Mo-CeO_2 surface exhibits stable favorability, while kinetically, the process occurs through facile barrierless pathways. Therefore, the Mo center functions as efficient active site, simultaneously accelerating water dissociation kinetics and serving as an efficient source of reactive protons for ORR.

Building upon these findings, the mechanistic basis for enhanced catalytic activity of H_2O_2 generation via the $2e^-$ ORR in Mo-CeO_2 becomes evident through electronic structure analysis. The density of states (DOS) calculations for pristine CeO_2 and Mo-CeO_2 (111) surfaces reveal their critical modifications (Figs. 5(d)–5(g)). In pristine CeO_2 (111), the conduction band minimum (CBM) is dominated by unoccupied Ce_{4f} orbitals, while the valence band maximum (VBM) comprises O_{2p} states. The surface Ce^{4+} ions (Bader charge: +2.35), exhibiting minimal contribution near the VBM (Fig. 5(d), red), attain their maximum oxidation state, resulting in weak adsorption of oxygen-containing intermediates. For comparison, Mo introduction into CeO_2 induces a significant upward shift in the Fermi level (E_f). This modified electronic configuration of Mo-CeO_2 facilitates enhanced charge transfer kinetics, resulting in increased adsorption energy. Crucially, the VBM of the Mo-CeO_2 (111) surface is predominantly composed of occupied Ce_{4f} orbitals corresponding to surface Ce^{3+} species (Bader charge: +2.10; Fig. 5(d), green). This electronic restructuring promotes O_2 activation, a critical function given that the initial protonation step ($O_2 + H^+ + e^- \rightarrow OOH^*$) constitutes the kinetic bottleneck for the overall $2e^-$ ORR pathway. Notably, Mo doping stabilizes surface Ce^{3+} species (Figs. 5(e) and 5(f)), which reside 0.15 eV lower in energy than subsurface Ce^{3+}, in contrast to the case in pristine CeO_2 (Fig. S25 in the ESM). This thermodynamically favored configuration significantly enhances OOH^* adsorption energetics (Fig. 5(g)), ultimately elevating $2e^-$ ORR activity beyond the performance achievable with surface Ce^{4+} in pristine CeO_2.

To establish a quantitative correlation between electronic structure and intermediate stability, we computed ΔG_{OOH} and performed Bader charge analysis for *OOH on the respective surfaces (Table S6 in the ESM). The results demonstrate a distinct positive relationship: An increased net electron transfer from the catalyst to the *OOH intermediate correlates directly with a stronger adsorption energy. On pristine CeO_2, the charge transfer is negligible (−0.13|e|), consistent with the charge density difference plots (Figs. S27(a) and S27(b) in the ESM) where OOH persists as a radical species featuring an unpaired electron. In sharp contrast, adsorption on the Mo-CeO_2 surface induces a substantial charge transfer of −0.62|e|. This pronounced charge redistribution, visually apparent in Figs. S27(c) and S27(d) in the ESM, signify the stabilization of OOH as an anionic species (OOH^-), characterized by the localization of an electron pair in the O–O π orbital. This quantitative electronic descriptor bridges the optimized configuration of the Mo–Ce dual site with its thermodynamically favorable ΔG_{OOH} (−0.51 eV, Fig. 5(c)), thereby providing a coherent theoretical rationale for the superior experimental 2e⁻ ORR selectivity and activity observed for the Mo-CeO_2 catalyst.

3 Conclusions

In conclusion, an efficient approach to electrocatalytic H_2O_2 synthesis through atomically engineered Mo-CeO_2 catalysts featuring oxygen vacancy-mediated Mo–Ce dual-active sites is demonstrated. By strategically incorporating Mo into the ceria lattice via hydrothermal defect engineering, synergistic sites that fundamentally resolve the persistent activity–selectivity tradeoff in 2e⁻ ORR are created. Advanced *in-situ* characterization and DFT calculations reveal three functions of Mo-CeO_2: (i) the unique hollow adsorption geometry, where the *OOH intermediate bridges the *in-situ* generated Mo and adjacent Ce atoms, stabilizes *OOH intermediates (ΔG_{OOH} = −0.51 eV) on the Mo-CeO_2 surface; (ii) Mo sites spontaneously dissociate water to supply protons while adjacent Ce centers optimize O_2 adsorption configurations; and (iii) critically, this dual-site cooperativity thereby disrupts the conventional scaling relationship between O_2 adsorption strength and *OOH binding energy. The strategically modified architecture demonstrates exceptional capability in steering the 2e⁻ ORR, achieving a notable H_2O_2 production rate of 8.2 $mol \cdot g_{cat}^{-1} \cdot h^{-1}$ at 100 $mA \cdot cm^{-2}$, outperforming recently reported noble-metal-free catalysts. This work provides a universal design framework for transition metal oxide catalysts, demonstrating how targeted dual-site engineering can simultaneously control intermediate stabilization, proton transfer kinetics, and reaction pathway selectivity for complex multi-electron transformations.

Electronic Supplementary Material: Supplementary material (material preparation methods, electrochemical measurement methods, theoretical calculation methods, figures, and tables) is available in the online version of this article at https://doi.org/10.26599/NR.2026.94908639.

Data availability

All data needed to support the conclusions in the paper are presented in the manuscript and the Electronic Supplementary Material. Additional data related to this paper may be requested from the corresponding author upon request.

Acknowledgements

This study was supported by the National Key R&D Program of China (No. 2021YFA1500700), the National Natural Science Foundation of China (Nos. 52472131, 52502145, 52302058, and 22473043), and Excellent Youth Research Project of Anhui Province Scientific Research Planning (No. 2024AH030043). The authors thank the Research Center of Analysis and Test of East China University of Science and Technology and the Feringa Nobel Prize Scientist Joint Research Center for the characterizations.

Declaration of competing interest

All the contributing authors report no conflict of interests in this work.

Author contribution statement

S. G.: Writing – original draft, funding acquisition, investigation, validation. X. L.: Writing – original draft, data curation, conceptualization, visualization. W. X. L.: Writing – original draft, formal analysis, methodology, validation. R. J. X.: Investigation, visualization. J. L. W.: Methodology, validation. J. L.: Investigation, resources, writing – review & editing. J. F. C.: Funding acquisition, methodology, software, writing – review & editing. H. H. W.: Funding acquisition, project administration, supervision, writing – review & editing. W. D.: Funding acquisition, supervision, writing – review & editing. All the authors have approved the final manuscript.

Use of AI statement

None.

References

[1] Wang, R. L.; Luo, H.; Duan, C. Y.; Liu, H. M.; Sun, M. D.; Zhou, Q.; Ou, Z. S.; Lu, Y. L.; Luo, G. H.; Yu, J. C. et al. Crystal OH mediating pathway for hydrogen peroxide production via two-electron water oxidation in non-carbonate electrolytes. *Nat. Commun.* **2024**, *15*, 10456.

[2] Huang, H. L.; Sun, M. Z.; Li, S. W.; Zhang, S. B.; Lee, Y.; Li, Z. W.; Fang, J. J.; Chen, C. J.; Zhang, Y. X.; Wu, Y. F. et al. Enhancing H_2O_2 electrosynthesis at industrial-relevant current in acidic media on diatomic cobalt sites. *J. Am. Chem. Soc.* **2024**, *146*, 9434–9443.

[3] Qian, J. N.; Liu, W.; Jiang, Y. T.; Mu, Y. B.; Cai, Y. Y.; Shi, L.; Zeng, L. Enhanced catalytic performance in two-electron oxygen reduction reaction via $ZnSnO_3$ perovskite. *ACS Sustain. Chem. Eng.* **2022**, *10*, 14351–14360.

[4] Peng, W.; Liu, J. X.; Liu, X. Q.; Wang, L. Q.; Yin, L. C.; Tan, H. T.; Hou, F.; Liang, J. Facilitating two-electron oxygen reduction with pyrrolic nitrogen sites for electrochemical hydrogen peroxide production. *Nat. Commun.* **2023**, *14*, 4430.

[5] Campos-Martin, J. M.; Blanco-Brieva, G.; Fierro, J. L. G. Hydrogen peroxide synthesis: An outlook beyond the anthraquinone process. *Angew. Chem., Int. Ed.* **2006**, *45*, 6962–6984.

[6] He, H. J.; Liu, S. L.; Liu, Y. Y.; Zhou, L. M.; Wen, H.; Shen, R. F.; Zhang, H. H.; Guo, X. J.; Jiang, J. C.; Li, B. J. Review and perspectives on carbon-based electrocatalysts for the production of H_2O_2 via two-electron oxygen reduction. *Green Chem.* **2023**, *25*, 9501–9542.

[7] Wang, Q.; Ren, L. P.; Zhang, J.; Chen, X.; Chen, C. Y.; Zhang, F.; Wang, S.; Chen, J.; Wei, J. J. Recent progress on the catalysts and device designs for (photo)electrochemical on-site H_2O_2 production. *Adv. Energy Mater.* **2023**, *13*, 2301543.

[8] Chen, S. Y.; Luo, T.; Wang, J. Y.; Xiang, J. Q.; Li, X. Q.; Ma, C.; Kao, C. W.; Chan, T. S.; Liu, Y. N.; Liu, M. Tuning proton affinity on Co–N–C atomic interface to disentangle activity–selectivity tradeoff in acidic oxygen reduction to H_2O_2. *Angew. Chem., Int. Ed.* **2025**, *64*, e202418713.

[9] Wen, Z. Y.; Han, N.; Li, Y. G. Recent progress towards the production of H_2O_2 by electrochemical two-electron oxygen reduction reaction. *Acta Phys.-Chim. Sin.* **2024**, *40*, 2304001.

[10] Li, G.; Wang, P.; He, M.; Yuan, X. L.; Tang, L. L.; Li, Z. X. Cerium-based nanomaterials for photo/electrocatalysis. *Sci. China Chem.* **2023**, *66*, 2204–2220.

[11] Dong, Z. Q.; Zhou, C. H.; Chen, W. B.; Lin, F. X.; Luo, H.; Sun, Z. Q.; Huang, Q. Z.; Zeng, R. J.; Tan, Y. J.; Xiao, Z. H. et al. Cerium dioxide as an electron buffer to stabilize iridium for efficient water electrolysis. *Adv. Funct. Mater.* **2024**, *34*, 2400809.

[12] Xue, L.; Zhang, C. J.; Wu, J. F.; Fan, Q. Y.; Liu, Y.; Wu, Y. X.; Li, J. X.; Zhang, H.; Liu, F. R.; Zeng, S. H. Unveiling the reaction pathway on Cu/CeO_2 catalyst for electrocatalytic CO_2 reduction to CH_4. *Appl. Catal. B: Environ.* **2022**, *304*, 120951.

[13] Zhou, X. L.; Shan, J. Q.; Chen, L.; Xia, B. Y.; Ling, T.; Duan, J. J.; Jiao, Y.; Zheng, Y.; Qiao, S. Z. Stabilizing Cu^{2+} ions by solid solutions to promote CO_2 electroreduction to methane. *J. Am. Chem. Soc.* **2022**, *144*, 2079–2084.

[14] Yin, H. B.; Chen, Z.; Peng, Y.; Xiong, S. C.; Li, Y. D.; Yamashita, H.; Li, J. H. Dual active centers bridged by oxygen vacancies of ruthenium single-atom hybrids supported on molybdenum oxide for photocatalytic ammonia synthesis. *Angew. Chem., Int. Ed.* **2022**, *61*, e202114242.

[15] Fan, C. M.; Dou, S. X.; Zhan, X. Q.; Li, S. G.; Wang, Q.; Li, B. Molten-salt electrochemical-assisted synthesis of the CeO_2–O_V@GC composite-supported Pt clusters with a Pt–O–Ce structure for the oxygen reduction reaction. *Nano Lett.* **2024**, *24*, 6957–6964.

[16] Cao, X. M.; Chen, J. Q.; Zhao, X. R.; Ge, H.; Liu, D. L.; Wu, Q.; Sun, Z. J.; Zhang, Q. G. Facile synthesis of bead-chain structured MWCNTs@CeO_2 with oxygen vacancies-rich for promoting electrochemical energy storage. *Chem. Eng. J.* **2024**, *479*, 147663.

[17] Xiao, Y. H.; Tan, X. H.; Guo, Y. Y.; Chen, J. P.; He, W. D.; Cui, H.; Wang, C. X. Surface modification of CeO_{2-x} nanorods with Sn doping for enhanced nitrogen electroreduction. *J. Energy Chem.* **2023**, *87*, 400–407.

[18] Sun, G. R.; Liu, X. B.; Mao, H. M.; Wu, S. Q.; Liu, Y. R.; Wang, T. S.; Chi, J. Q.; Wang, L. Highly efficient tungsten/molybdenum-based electrocatalysts for the oxygen reduction reaction: A review. *Inorg. Chem. Front.* **2024**, *11*, 682–712.

[19] Tang, C.; Jiao, Y.; Shi, B. Y.; Liu, J. N.; Xie, Z. H.; Chen, X.; Zhang, Q.; Qiao, S. Z. Coordination tunes selectivity: Two-electron oxygen reduction on high-loading molybdenum single-atom catalysts. *Angew. Chem., Int. Ed.* **2020**, *59*, 9171–9176.

[20] Zhao, X.; Wang, Y.; Da, Y. L.; Wang, X. X.; Wang, T. T.; Xu, M. Q.; He, X. Y.; Zhou, W.; Li, Y. F.; Coleman, J. N. et al. Selective electrochemical production of hydrogen peroxide at zigzag edges of exfoliated molybdenum telluride nanoflakes. *Natl. Sci. Rev.* **2020**, *7*, 1360–1366.

[21] Yang, W. P.; Qi, F. Y.; An, W. J.; Yu, H. C.; Liu, S. T.; Ma, P. P.; Chen, R.; Liu, S. X.; Lou, L. L.; Yu, K. Local electronic structure modulation of interfacial oxygen vacancies promotes the oxygen activation capacity of Pt/$Ce_{1-x}M_xO_{2-\delta}$. *ACS Catal.* **2024**, *14*, 5936–5948.

[22] Xiong, T. Z.; Huang, B. W.; Wei, J. J.; Yao, X. C.; Xiao, R.; Zhu, Z. X.; Yang, F.; Huang, Y. C.; Yang, H.; Balogun, M. S. Unveiling the promotion of accelerated water dissociation kinetics on the hydrogen evolution catalysis of $NiMoO_4$ nanorods. *J. Energy Chem.* **2022**, *67*, 805–813.

[23] Hu, Y. Z.; Zhang, J. J.; Shen, T.; Li, Z. R.; Chen, K.; Lu, Y.; Zhang, J.; Wang, D. L. Efficient electrochemical production of H_2O_2 on hollow N-doped carbon nanospheres with abundant micropores. *ACS Appl. Mater. Interfaces* **2021**, *13*, 29551–29557.

[24] Yan, M. M.; Wei, Z. X.; Gong, Z. C.; Johannessen, B.; Ye, G. L.; He, G. C.; Liu, J. J.; Zhao, S. L.; Cui, C. Y.; Fei, H. L. Sb_2S_3-templated synthesis of sulfur-doped Sb–N–C with hierarchical architecture and high metal loading for H_2O_2 electrosynthesis. *Nat. Commun.* **2023**, *14*, 368.

[25] Geng, Y.; Jin, K.; Mei, J.; Su, G. Y.; Ma, L.; Yang, S. J. CeO_2 grafted with different heteropoly acids for selective catalytic reduction of NO_x with NH_3. *J. Hazard. Mater.* **2020**, *382*, 121032.

[26] Liao, X.; Zhang, Y.; Guo, J. Q.; Zhao, L. L.; Hill, M.; Jiang, Z.; Zhao, Y. X. The catalytic hydrogenation of maleic anhydride on $CeO_{2-\delta}$-supported transition metal catalysts. *Catalysts* **2017**, *7*, 272.

[27] Qu, Z. P.; Yu, F. L.; Zhang, X. D.; Wang, Y.; Gao, J. S. Support effects on the structure and catalytic activity of mesoporous Ag/CeO_2 catalysts for CO oxidation. *Chem. Eng. J.* **2013**, *229*, 522–532.

[28] Yang, S.; Zhu, X. Y.; Chen, S. R.; Zhu, X. C.; Liu, H.; Chen, J. J.; Chen, D. Z.; Sun, C. Z.; Li, J. H. Hexavalent metal cations doped into ceria inducing the formation of binuclear sites Ce^{3+}–O–Ce^{3+} to boost the NH_3-SCR reaction. *ACS Catal.* **2024**, *14*, 7277–7288.

[29] Chen, H. J.; Xu, R. H.; Chen, D.; Lu, T. L.; Li, H. J.; Wang, M. Subsurface Mo vacancy in bismuth molybdate promotes photocatalytic oxidation of lactate to pyruvate. *ACS Catal.* **2024**, *14*, 1977–1986.

[30] Qin, S.; Chen, Q.; Huang, C.; Li, J. Q.; Shi, Y. Z.; Cui, X. W.; Wang, Z. W.; Song, Y. J.; Wu, L. Construction of 3D/2D CeO_2/Bi_2MoO_6 S-scheme heterojunction for photocatalytic cascade reactions of secondary amines synthesis. *Rare Met.* **2025**, *44*, 10306–10320.

[31] Yang, Q. Y.; Sun, C. H.; Sun, L. J.; Liu, H. N.; Su, L. H.; Ma, C. L.; Wang, J.; Gong, L. Y.; Yan, Z. H. Homogeneous bismuth dopants regulate cerium oxide structure to boost hydrogen peroxide electrosynthesis via two-electron oxygen reduction. *Inorg. Chem. Front.* **2025**, *12*, 3384–3392.

[32] Liu, H.; Li, Y. L.; Qian, Y. Y.; Tong, Y. S.; Yang, Q. H.; Wang, J. G.; Su, D. S.; Zhao, Y. Y.; Tian, Z. Q.; Lu, Z. Y. et al. Unveiling the mechanism of photocatalytic CO_2 cycloaddition over linker‐engineered metal‐organic frameworks. *Angew. Chem., Int. Ed.* **2026**, *65*, e25369.

[33] Jiang, R. M.; Yue, X. Y.; Wang, K.; Yang, Z.; Dai, W. X.; Fu, X. Z. Photothermal-catalyzing CO_2 methanation over different-shaped CeO_2-based Ru nanoparticles. *Energy Fuels* **2022**, *36*, 11636–11646.

[34] Drouilly, C.; Krafft, J. M.; Averseng, F.; Casale, S.; Bazer-Bachi, D.; Chizallet, C.; Lecocq, V.; Vezin, H.; Lauron-Pernot, H.; Costentin, G. ZnO oxygen vacancies formation and filling followed by *in-situ* photoluminescence and *in-situ* EPR. *J. Phys. Chem. C* **2012**, *116*, 21297–21307.

[35] Trabelsi, H.; Bejar, M.; Dhahri, E.; Graça, M. P. F.; Valente, M. A.; Soares, M. J.; Sobolev, N. A. Raman, EPR and ethanol sensing properties of oxygen-vacancies $SrTiO_{3-\delta}$ compounds. *Appl. Surf. Sci.* **2017**, *426*, 386–390.

[36] Cheng, M.; Li, Z. G.; Xu, T. X.; Mao, Y. X.; Zhang, Y.; Zhang, G. X.; Yan, Z. F. Efficient overall $2e^-$ oxygen electrolysis to H_2O_2 on CeO_2 nanocubes. *Electrochim. Acta* **2022**, *430*, 141091.

[37] Dong, K.; Liang, J.; Wang, Y. Y.; Ren, Y. C.; Xu, Z. Q.; Zhou, H. P.; Li, L.; Liu, Q.; Luo, Y. L.; Li, T. S. et al. Plasma-induced defective TiO_{2-x} with oxygen vacancies: A high-active and robust bifunctional catalyst toward H_2O_2 electrosynthesis. *Chem Catal.* **2021**, *1*, 1437–1448.

[38] Zhang, C. Q.; Yuan, L.; Liu, C.; Li, Z. M.; Zou, Y. Y.; Zhang, X. C.; Zhang, Y.; Zhang, Z. Q.; Wei, G. F.; Yu, C. Z. Crystal engineering enables cobalt-based metal–organic frameworks as high-performance electrocatalysts for H_2O_2 production. *J. Am. Chem. Soc.* **2023**, *145*, 7791–7799.

[39] Sun, Y. Y.; Sinev, I.; Ju, W.; Bergmann, A.; Dresp, S.; Kühl, S.; Spöri, C.; Schmies, H.; Wang, H.; Bernsmeier, D. et al. Efficient

electrochemical hydrogen peroxide production from molecular oxygen on nitrogen-doped mesoporous carbon catalysts. *ACS Catal.* **2018**, *8*, 2844–2856.

[40] Zhang, H. X.; Yang, S. C.; Wang, Y. L.; Xi, J. C.; Huang, J. C.; Li, J. F.; Chen, P.; Jia, R. Electrocatalyst derived from fungal hyphae and its excellent activity for electrochemical production of hydrogen peroxide. *Electrochim. Acta* **2019**, *308*, 74–82.

[41] Deng, Z. Q.; Ma, C. Q.; Yan, S. H.; Liang, J.; Dong, K.; Li, T. S.; Wang, Y.; Yue, L. C.; Luo, Y. L.; Liu, Q. et al. Electrocatalytic H_2O_2 production via two-electron O_2 reduction by Mo-doped TiO_2 nanocrystallines. *Catal. Sci. Technol.* **2021**, *11*, 6970–6974.

[42] Chai, X. C.; Gao, R. T.; Wang, L. Electron transport kinetics via ZnO with ultralow Fe dopant for stable oxygen reduction to H_2O_2. *Chem. Eng. J.* **2024**, *484*, 149527.

[43] Wu, J.; Han, Y. D.; Bai, Y. C.; Wang, X. T.; Zhou, Y. J.; Zhu, W. X.; He, T. W.; Wang, Y. M.; Huang, H.; Liu, Y. et al. The electron transport regulation in carbon dots/In_2O_3 electrocatalyst enable 100% selectivity for oxygen reduction to hydrogen peroxide. *Adv. Funct. Mater.* **2022**, *32*, 2203647.

[44] Xu, S. R.; Yu, Y.; Zhang, X. Y.; Xue, D. P.; Wei, Y. F.; Xia, H. C.; Zhang, F. X.; Zhang, J. N. Enhanced electron delocalization induced by ferromagnetic sulfur doped C_3N_4 triggers selective H_2O_2 production. *Angew. Chem., Int. Ed.* **2024**, *63*, e202407578.

[45] Zhang, J. Y.; Zhang, G.; Jin, S. Y.; Zhou, Y. J.; Ji, Q. H.; Lan, H. C.; Liu, H. J.; Qu, J. H. Graphitic N in nitrogen-doped carbon promotes hydrogen peroxide synthesis from electrocatalytic oxygen reduction. *Carbon* **2020**, *163*, 154–161.

[46] Zhang, F. F.; Zhu, Y. L.; Tang, C.; Chen, Y.; Qian, B. B.; Hu, Z. W.; Chang, Y. C.; Pao, C. W.; Lin, Q.; Kazemi, S. A. et al. High-efficiency electrosynthesis of hydrogen peroxide from oxygen reduction enabled by a tungsten single atom catalyst with unique terdentate N_1O_2 coordination. *Adv. Funct. Mater.* **2022**, *32*, 2110224.

[47] Wang, Y. L.; Shi, R.; Shang, L.; Waterhouse, G. I. N.; Zhao, J. Q.; Zhang, Q. H.; Gu, L.; Zhang, T. R. High-efficiency oxygen reduction to hydrogen peroxide catalyzed by nickel single-atom catalysts with tetradentate N_2O_2 coordination in a three-phase flow cell. *Angew. Chem., Int. Ed.* **2020**, *59*, 13057–13062.

[48] Zhou, Y. J.; Xu, L.; Wu, J.; Zhu, W. X.; He, T. W.; Yang, H.; Huang, H.; Cheng, T.; Liu, Y.; Kang, Z. H. The operation active sites of O_2 reduction to H_2O_2 over ZnO. *Energy Environ. Sci.* **2023**, *16*, 3526–3533.

[49] Li, R. L.; Yang, S. K.; Zhang, Y. D.; Yu, G.; Wang, C.; Chen, C.; Wu, G.; Sun, R. B.; Wang, G. Z.; Zheng, X. S. et al. Short-range order in amorphous nickel oxide nanosheets enables selective and efficient electrochemical hydrogen peroxide production. *Cell Rep. Phys. Sci.* **2022**, *3*, 100788.

[50] Dong, K.; Xu, Z. Q.; He, X.; Zhao, D. L.; Chen, H. J.; Liang, J.; Luo, Y. S.; Sun, S. J.; Zheng, D. D.; Liu, Q. et al. Ultrathin single-crystal $PtSe_2$ nanosheets for high-efficiency O_2 electroreduction to H_2O_2. *Chem. Commun.* **2022**, *58*, 10683–10686.

[51] Xie, L. P.; Liang, C. H.; Wu, Y.; Wang, K.; Hou, W. D.; Guo, H. Z.; Wang, Z. M.; Lam, Y. M.; Liu, Z.; Wang, L. Isomerization engineering of oxygen-enriched carbon quantum dots for efficient electrochemical hydrogen peroxide production. *Small* **2024**, *20*, 2401253.

[52] Sun, Q. D.; Yue, X.; Yu, L. K.; Li, F. Z.; Zheng, Y. W.; Liu, M. T.; Peng, J. Z.; Hu, X. L.; Chen, H. M.; Li, L. et al. Well-defined Co_2 dual-atom catalyst breaks scaling relations of oxygen reduction reaction. *J. Am. Chem. Soc.* **2024**, *146*, 35295–35304.

[53] Jia, B. B.; Xie, X.; Lin, J.; Wang, H. Q.; Hu, P. F.; Wang, F. Y.; Fan, X. Y.; Zheng, J. L.; Ma, T. Y.; Ye, L. Q. Harnessing pyridinic N vacancy defect in microporous structures to induce the pre‐adsorption of oxygen and boost oxygen reduction reaction kinetics. *Angew. Chem., Int. Ed.* **2025**, *64*, e202508674.

[54] Chen, S. Y.; Luo, T.; Li, X. Q.; Chen, K. J.; Fu, J. W.; Liu, K.; Cai, C.; Wang, Q. Y.; Li, H. M.; Chen, Y. et al. Identification of the highly active Co–N_4 coordination motif for selective oxygen reduction to hydrogen peroxide. *J. Am. Chem. Soc.* **2022**, *144*, 14505–14516.

[55] Chai, M. Q.; Xing, R. J.; Chen, J. F.; Su, Z. X.; Wei, H. H.; Zhu, H. W.; Gong, X. Q. Atomic Pd sites on CeO_2 nanorods for highly selective hydrogen peroxide generation and efficient degradation of organic pollutants. *ACS Sustain. Chem. Eng.* **2025**, *13*, 1391–1400.

[56] Zhou, C. A.; Ma, K.; Zhuang, Z. C.; Ran, M. L.; Shu, G. Q.; Wang, C.; Song, L.; Zheng, L. R.; Yue, H. R.; Wang, D. S. Tuning the local environment of Pt species at CNT@MO_{2-x} (M = Sn and Ce) heterointerfaces for boosted alkaline hydrogen evolution. *J. Am. Chem. Soc.* **2024**, *146*, 21453–21465.